

# Superconductivity in bismuth pyrochlore lattice compounds $\text{RbBi}_2$ and $\text{CsBi}_2$ : the role of relativistic effects

Sylvia Gutowska<sup>†</sup>, Bartłomiej Wiendlocha<sup>†</sup>, Tomasz Klimczuk<sup>‡</sup>, Michał J. Winiarski<sup>‡,\*</sup>

<sup>†</sup> Faculty of Physics and Applied Computer Science, AGH University of Science and Technology, Aleja Mickiewicza 30, 30-059 Kraków, Poland

<sup>‡</sup> Faculty of Applied Physics and Mathematics and Advanced Materials Center, Gdansk University of Technology, ul. Narutowicza 11/12, 80-233 Gdansk, Poland

**ABSTRACT:** Superconducting properties of two bismuthide intermetallic compounds,  $\text{RbBi}_2$  and  $\text{CsBi}_2$ , were studied by means of experimental measurements and *ab initio* calculations. We show that in both compounds the superconductivity emerges from the pyrochlore Bi lattice and its formation is heavily influenced by relativistic effects. Based on our analysis of the effect of spin-orbit coupling on the electron-phonon coupling we suggest a possible criterion for finding new superconducting materials by looking for structures featuring relativistically-stabilized hypervalent networks of heavy *p*-block elements.

## INTRODUCTION

Bismuth is the heaviest stable element of the periodic table (the half-life of  $^{209}\text{Bi}$   $\tau_{1/2} = 2.0 \times 10^{19}$  yr is nine orders of magnitude longer than the age of the universe,  $t = 1.4 \times 10^{10}$  yr). This property makes it and its compounds interesting for studying effects of strong spin orbit coupling (SOC) on physical properties of materials. Relativistic effects often result in Bi compounds behaving differently than isoelectronic species. For example, the most common cationic oxidation state of Bi is +3, with +5 compounds being generally unstable towards reduction.  $\text{Bi}^{3+}$  cation is very often lone-pair active, leading to complicated coordination environments. Less known are the effects of relativistic phenomena on structural chemistry of Bi intermetallic compounds. Bi is known to form several stable hypervalent polyanions, such as  $\text{Bi}^-$  square network found in  $\text{LiBi}$  and  $\text{NaBi}$  but not observed in the isoelectronic  $\text{NaSb}^{1-4}$ . Similarly,  $\text{CaBi}_2$  and the recently reported  $\text{SrBi}_2$  both host a hypervalent  $\text{Bi}^-$  square lattice<sup>5,6</sup>, which is missing in the isoelectronic  $\text{CaSb}_2$ <sup>7</sup>.

A number of binary bismuth superconductors are known, including:  $\text{Ca}_{11}\text{Bi}_{10-x}$ <sup>8</sup>,  $\text{CaBi}_2$ <sup>9,10</sup>,  $\text{SrBi}_3$ <sup>11,12</sup>,  $\text{BaBi}_3$ <sup>13</sup>,  $\text{Ba}_2\text{Bi}_3$ <sup>14</sup>,  $\text{LiBi}$ <sup>4,15</sup>,  $\text{NaBi}$ <sup>3</sup>,  $\text{KBi}_2$ <sup>16-18</sup>,  $\text{RbBi}_2$ <sup>18</sup>, and  $\text{CsBi}_2$ <sup>19</sup>. The latter three compounds are cubic Laves phases, crystallizing in a relatively simple  $\text{MgCu}_2$ -type structure in which Bi atoms form a pyrochlore (vertex sharing tetrahedral) network (Fig. 1). Interestingly, while the  $\text{MgCu}_2$  is the 5<sup>th</sup> most common binary intermetallic structure type<sup>20</sup>, only a few of the known compounds feature a *p*-block element occupying the pyrochlore network - besides the three dibismuthides, these are  $\text{MgIn}_2$ <sup>21</sup>,  $\text{SnS}_2$ <sup>22</sup>, and  $\text{RAl}_2$ , ( $R = \text{Sr}, \text{Ba}, \text{rare-earth metals}, \text{Th}, \text{U}$ ).

Here we present the results of our experimental and computational studies on  $\text{RbBi}_2$  and  $\text{CsBi}_2$ , concentrated on the effects of strong SOC on superconducting properties. We show that in both compounds superconductivity emerges from the  $\text{Bi}_4^{2-}$  pyrochlore lattice and that the relativistic effects play a complex role in stability and properties of the two phases. We found that strong SOC is crucial for the stability of charged Bi pyrochlore

network and discuss the implications of this fact for the search for new heavy element-bearing superconducting materials.

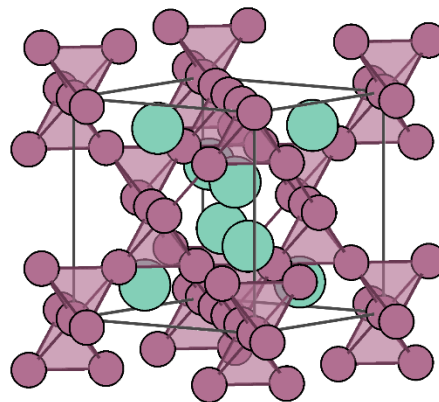


Figure 1. Crystal structure of the cubic Laves phases  $\text{ABi}_2$  ( $A = \text{K}, \text{Rb}, \text{Cs}$ ). Bi atoms (drawn in purple) form a vertex-sharing tetrahedral (pyrochlore) lattice with voids filled with alkali atoms (green).

## MATERIALS AND METHODS

Single crystals of  $\text{RbBi}_2$  and  $\text{CsBi}_2$  were grown using a Bi self-flux method. Pieces of bismuth (Alfa Aesar, 99.99%) and rubidium (Alfa Aesar, 99.9%) were put in an alumina crucible inside an Ar-filled glovebox. Cesium was first heated above its melting point by warming it in hand and then poured dropwise into the crucible and covered with Bi pieces. Crucibles were then put in fused silica tubes along with plugs of quartz wool, and the tubes were subsequently evacuated, back-filled with Ar, and sealed without exposing alkaline metals to air. They were then heated to 550°C, kept at that temperature for 8 hours, and then slowly cooled (5°C per hour) to 310°C at which temperature the excess Bi was spun off with the aid of a centrifuge. Clusters of octahedrally and tetrahedrally-shaped crystals were obtained, with sizes ranging up to ca. 1 mm. The phase identity

of the crystals was examined using powder x-ray diffraction (PXRD) measurements employing a Bruker D8 FOCUS diffractometer with a Cu  $K\alpha$  radiation source and a LynxEye detector. A few single crystals were crushed for the PXRD measurements inside an Ar-filled glovebox and mixed with an Apizon-N grease or petroleum jelly. Since the powdered samples quickly oxidize, reacting with oxygen and moisture from air, the scanning time had to be reduced to 8 min. PXRD patterns were then analyzed by means of the LeBail method<sup>23</sup> using the FullProf software package<sup>24</sup>. PXRD patterns taken after a prolonged exposition to air show that both compounds decomposed completely yielding weakly crystalline elemental Bi and an amorphous product (most probably a hydrated alkali metal hydroxide), similarly to what was observed in  $\text{CaBi}_2$ <sup>9</sup>.

Heat capacity measurements were performed using Quantum Design PPMS system by the standard relaxation technique. Magnetic susceptibility measurements were carried out using the ACMS option of the PPMS. Multiple randomly-oriented single crystals were put in the standard straw sample holders. Sample preparation was carried out inside a glovebox to prevent oxidation.

*Ab initio* calculations were performed using the Quantum Espresso (QE) package<sup>25</sup> employing ultrasoft Perdew-Burke-Ernzerhof (PBE) GGA<sup>26</sup> pseudopotentials<sup>27</sup> with valence configuration  $4s^25s^4p^6$  for Rubidium,  $5s^26s^15p^6$  for Cesium and  $6s^26p^35d^{10}$  for Bismuth, whereas the wavefunction and charge density energy cut-off's were set to values 50 Ry and 500 Ry, respectively. For the consideration of the influence of the relativistic effects, two types of calculations were performed: scalar-relativistic (neglecting SOC) and fully-relativistic (with SOC effect included for Bi). As expected and tested, inclusion of SOC for Rb and Cs does not change the results of calculations, thus the SOC was include only for Bi in final calculations. In the first step lattice constant was optimized using the Broyden-Fletcher-Shanno-Goldfarb (BFGS) method. The electronic structure was calculated at the grid of  $(24)^3$  k-points. Phonon structure and properties of electron-phonon coupling (EPC) were calculated at grid of  $(6)^3$  q-points.

Chemical bonding was investigated by means of Crystal Orbital Hamilton Population analysis<sup>28,29</sup> using the Stuttgart TB-LMTO-ASA code<sup>30,31</sup>. Calculations were performed using the experimental cell parameter and  $(32)^3$  k-point mesh and employed the Perdew-Wang GGA<sup>32</sup> exchange-correlation ( $xc$ ) potential.

Electronic structure of an isolated tetrahedral  $\text{Bi}_4$  cluster was calculated using the ReSpect 5.1.0 relativistic DFT code<sup>33</sup>. Scalar-relativistic calculations were performed by means of 1-component Kohn-Sham method with one-electron relativistic corrections due to Douglas-Kroll-Hess of second order (1c KS-DKH2). Fully relativistic electronic structure was calculated using the four-component Dirac-Kohn-Sham Hamiltonian (4c DKS). The Dyll core-valence double-zeta basis set<sup>34</sup> and the PBE  $xc$  potential were used in both cases. Molecular orbitals obtained from the 1c KS-DKH2 calculations were visualized using the IboView program<sup>35,36</sup>.

## RESULTS AND DISCUSSION

Room temperature PXRD patterns of crushed crystals are presented in Fig. S1 of the Supplementary Material. All the Bragg lines in the PXRD pattern can be indexed to cubic (space group  $Fd\bar{3}m$ , #227) unit cell of  $\text{ABi}_2$  and elemental Bi (both from left-

over flux droplets and decomposition of material). Lattice parameters resulting from LeBail fits are in agreement with previous reports<sup>37,38</sup>. Details of crystal structures are gathered in Table 1.

The Rb-Rb and Cs-Cs distances are 4.20 Å and 4.26 Å, significantly shorter than in their elemental form (4.89 Å and 5.29 Å, respectively<sup>39,40</sup>), while Bi-Bi spacing is larger than in elemental Bi (3.47 Å vs. 3.07 Å<sup>41</sup>) and in the  $\text{Bi}_4$  cluster (2.98 Å as obtained by *ab initio* structural relaxation). This highlights the electron transfer from the electropositive alkali metal to the Bi network.

To characterize superconducting transitions of  $\text{ABi}_2$ , dc magnetization was measured in the temperature interval  $T = 1.9 \text{ K} - 5 \text{ K}$ . The plot of low-field ( $H_{dc} = 20 \text{ Oe}$ ) volume susceptibility ( $\chi_V$ ) vs. temperature is shown in Fig. 2(a,b). Sharp transition to a full Meissner state ( $\chi_V$  reaching the value of  $-4\pi$  after correcting for the demagnetization effect) was observed in both materials. Very small difference between zero-field cooled (ZFC) and field-cooled (FC) magnetization (not shown) is indicative of weak (or nonexistent) vortex pinning.

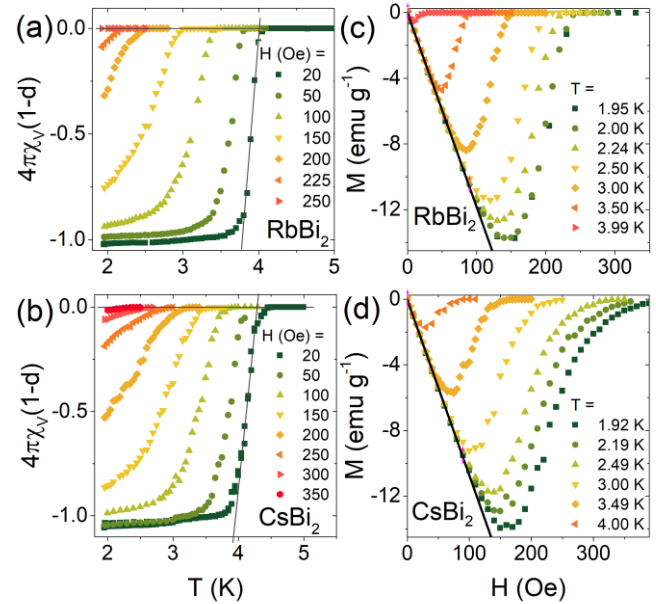


Fig. 2 (a,b) Temperature-dependent magnetic susceptibility of  $\text{RbBi}_2$  and  $\text{CsBi}_2$ . A sharp transition to Meissner state is seen at the  $T_c$ . Susceptibility data was corrected for the demagnetization factor (see the text). (c,d) Field-dependent magnetization curves showing a typical type-I character of superconductivity for  $\text{RbBi}_2$  and a probable type-II character for  $\text{CsBi}_2$ .

Field-dependent magnetization below the critical temperature is shown in Fig. 2(c,d). In case of  $\text{RbBi}_2$  the shape of magnetization curve is consistent with a type-I superconducting transition with an influence of the demagnetization effect due to randomly-oriented crystalline grains<sup>9,42</sup>. In  $\text{CsBi}_2$  the shape of the  $M$  vs.  $H$  curve has a tail-like feature at higher fields, which is more consistent with type-II SC. Assuming a perfect diamagnetic linear response to the magnetic field, the  $M_v$  vs  $H$  data at the lowest temperature ( $T = 1.92 \text{ K}$  and  $T = 1.95 \text{ K}$  for Rb- and Cs-bearing compound, respectively) was fitted with a linear function ( $M_{fit} = aH + b$ ). The value of the demagnetization factor ( $d$ ) is calculated using the equation  $-a = (4\pi(1-d))^{-1}$ , yielding  $d = 0.676$  for  $\text{RbBi}_2$  and  $d = 0.744$  for  $\text{CsBi}_2$ .

The fields at which deviations from a linear response occur were taken as thermodynamic critical fields  $H_c^*$ . The  $H_c^*$  values derived for different temperatures are fitted with the equation  $H_c^*(T) = H_c^*(0)[1 - (T/T_c)^2]^{43}$ . The value of critical field extrapolated to  $T = 0$  K using the fitted function is  $H_c^*(0) = 127$  Oe for  $\text{RbBi}_2$  and  $H_c^*(0) = 146$  Oe for  $\text{CsBi}_2$  (see Fig. S2 of the Supplementary Material). This value has to be corrected for the demagnetization factor, yielding  $H_c(0) = 188$  Oe and 196 Oe, respectively.

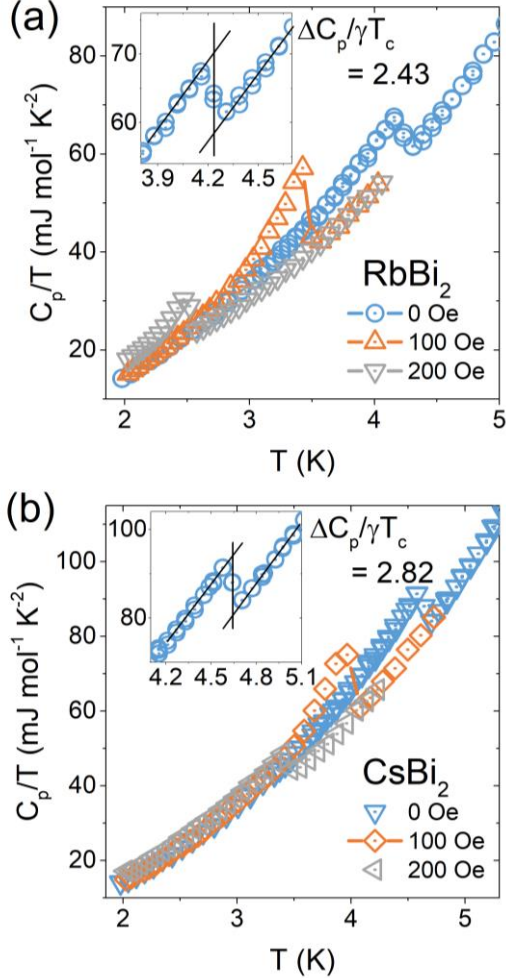


Fig. 3 Low temperature heat capacity of (a)  $\text{RbBi}_2$  and (b)  $\text{CsBi}_2$ , showing an anomaly at the superconducting critical temperature (enlarged in insets). The normalized heat capacity jump  $\Delta C_p/\gamma T_c$  is calculated using  $\gamma$  values estimated from a fit presented in Fig. S2 of the Supplementary Material. Note that in both cases the jump under an applied magnetic field is found to be larger than at zero field, which is a typical behavior for type-I superconductors (see eg. refs. <sup>16,44-47</sup>).

The heat capacity measured through the superconducting transition in  $\text{ABi}_2$  is shown in Fig. 3. Bulk nature of the superconductivity is confirmed by large, sharp anomalies at  $T_c = 4.24$  and 4.65 K for  $\text{RbBi}_2$  and  $\text{CsBi}_2$ , respectively. It is worth noting that under applied field the jump at  $T_c$  becomes larger than at zero field in both compounds. Similar effect was observed eg. in  $\text{KBi}_2$ <sup>16</sup>,  $\text{ScGa}_3$ ,  $\text{LuGa}_3$ <sup>44</sup>,  $\text{YbSb}_2$ <sup>45</sup>,  $\text{ReAl}_6$ <sup>46</sup>, and  $\text{LiPd}_2\text{Ge}$ <sup>47</sup> type-I superconductors.

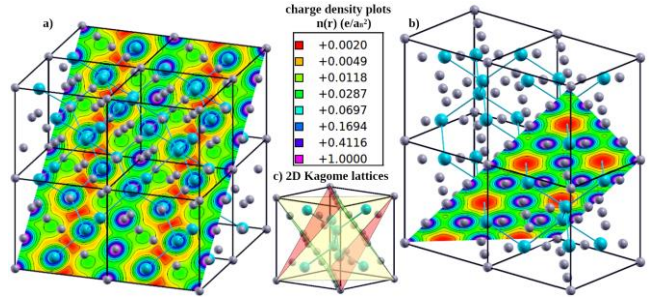


Fig. 4. Charge density of supercell of  $\text{RbBi}_2$  plotted in (110) plane (a) and (111) plane (b); the charge density in (111) plane is similar to 2D Kagome lattice marked, however there are many of such planes in unit cell (c) resulting in 3D character of electronic bonds.

Fig. S3 of the Supplementary Material presents the low-temperature  $C_p/T$  vs.  $T^2$  plots for both materials. Electronic ( $\gamma$ ) and vibrational ( $\beta$ ) heat capacity contributions were extracted by fitting the data with relation  $C_p/T = \gamma + \beta T^2$ . The fit yields very similar  $\gamma$  values (5.0 and 4.9  $\text{mJ mol}^{-1} \text{K}^{-2}$ ) for both materials. The normalized heat capacity jumps at  $T_c$  estimated by using the equal entropy construction method (see insets of Fig 5(a,b)), are  $\Delta C_p/\gamma T_c = 2.43$  for  $\text{RbBi}_2$  and  $\Delta C_p/\gamma T_c = 2.82$  for  $\text{CsBi}_2$ , both well above the BCS limit for a weakly-coupled superconductor (1.43).

The Debye temperature ( $\Theta_D$ ) is calculated from the  $\beta$  specific heat coefficients using the relation:

$$\Theta_D = \sqrt[3]{\frac{12\pi^4 nR}{5\beta}}$$

This yields  $\Theta_D = 127(1)$  for  $\text{RbBi}_2$  and 123(1) K for  $\text{CsBi}_2$ , both values being slightly higher than for elemental Bi ( $\Theta_D = 112$  K). Taking  $\Theta_D$  and  $T_c$  values and assuming the value of the Coulomb pseudopotential parameter  $\mu^* = 0.13$ , the electron-phonon coupling parameter ( $\lambda_{\text{el-ph}}$ ) can be calculated using the modified McMillan formula:

$$\lambda_{\text{el-ph}} = \frac{1.04 + \mu^* \ln\left(\frac{\Theta_D}{1.45T_c}\right)}{(1 - 0.62\mu^*) \ln\left(\frac{\Theta_D}{1.45T_c}\right) - 1.04}$$

For  $\text{RbBi}_2$  this gives  $\lambda_{\text{el-ph}} = 0.82$  and for  $\text{CsBi}_2$   $\lambda_{\text{el-ph}} = 0.87$ , both values being indicative of moderate coupling strength

Table 2 summarizes the normal and superconducting state parameters derived from experimental measurements.

Charge transfer from the Rb/Cs to Bi is evident from the electronic density of  $\text{RbBi}_2$  and  $\text{CsBi}_2$  (Fig. 4) and the Bader charge analysis yields  $\text{Rb}^{+0.71}(\text{Bi}_2)^{-0.71}$  and  $\text{Cs}^{+0.64}(\text{Bi}_2)^{-0.64}$ . This is consistent with electronegativity difference (0.82/0.79 vs. 2.02 for Rb/Cs and Bi in the Mulliken scale, respectively). The density distribution along the Bi-Bi bonds has a strongly delocalized, metallic character. Since charge density is concentrated on the Bi framework, both compounds can be viewed as pyrochlore metals.

**Table 2 Normal and superconducting state parameters for RbBi<sub>2</sub> and CsBi<sub>2</sub>**

	RbBi <sub>2</sub>	CsBi <sub>2</sub>
$\gamma$ (mJ mol <sup>-1</sup> K <sup>-2</sup> )	5.0(4)	4.9(2)
$\beta$ (mJ mol <sup>-1</sup> K <sup>-4</sup> )	2.83(3)	3.11(5)
Debye temp. $\Theta_D$ (K)	127(1)	123(1)
Critical temp. $T_c$ (K)	4.25	4.65
$\Delta C_p/\gamma T_c$	2.43	2.82
$\lambda_{el-ph}$	0.82	0.87
$H_c(0)$ (Oe)	188(1)	196(5)

The electronic band structure and electronic density of states (DOS) for both compounds are shown in Fig. 5. The band structure around the Fermi level is similar in both cases. The Fermi level lies within a peak of DOS, thus even a small difference of band structure detailed below, lead to higher DOS at Fermi level in case of CsBi<sub>2</sub> ( $DOS(E_F) = 1.51 \text{ eV}^{-1}/f.u.$ ) than RbBi<sub>2</sub> ( $DOS(E_F) = 1.31 \text{ eV}^{-1}/f.u.$ ), which is correlated with a higher transition temperature  $T_c$ , as discussed below.

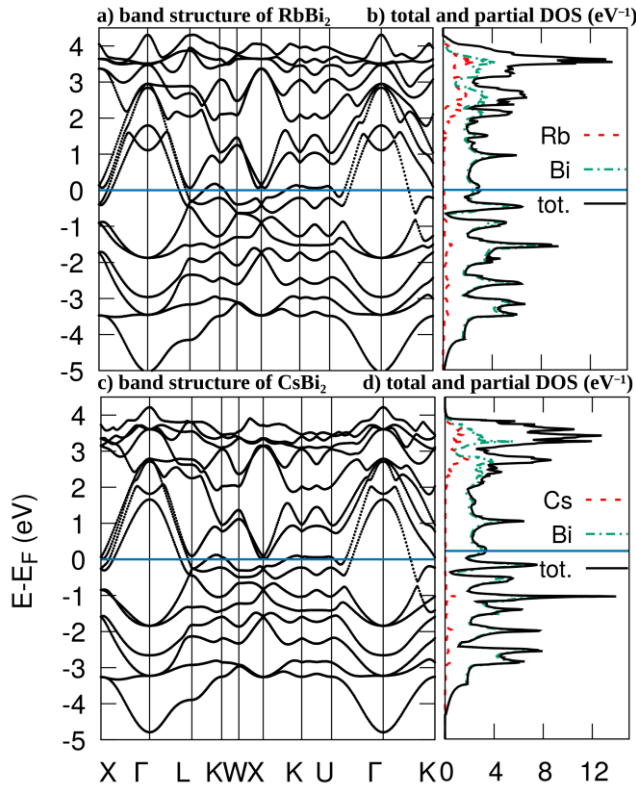


Fig. 5. Fully relativistic electronic band structure (a, c) and DOS (b, d) of RbBi<sub>2</sub> and CsBi<sub>2</sub> respectively. Atomic contributions to DOS are marked with green (Bi) and red (Rb/Cs) lines.

The plot of DOS shows that the  $p$ -states of Bi contribute the majority of the total DOS around Fermi level, being only slightly hybridized with  $s$  states of Rb/Cs. Bi  $6s$  states are positioned well below the  $E_F$  due to (scalar) relativistic effects<sup>48</sup>. Thus, both the metallic state and superconductivity in ABi<sub>2</sub> arises from interacting  $6p$  states of Bi atoms. In the energy range from -2.5 to 3 eV (with respect to  $E_F$ ) the shape of DOS is similar to the one of elemental bismuth. Particularly the minimum at -0.8 eV is similar to the one at Fermi level of pure Bi. Around

the  $E_F$  the DOS is similar to the case of elemental Bi under pressure  $p = 2.7 \text{ GPa}$ , at which a phase transition to a monoclinic structure is observed and Bi becomes superconducting below  $T_c = 3.9 \text{ K}$ <sup>49</sup>. In this sense, the presence of Rb/Cs atoms impose a chemical pressure on the lattice of Bi atoms, leading to stronger  $6p$  orbital overlap and metallic bonding of the Bi framework.

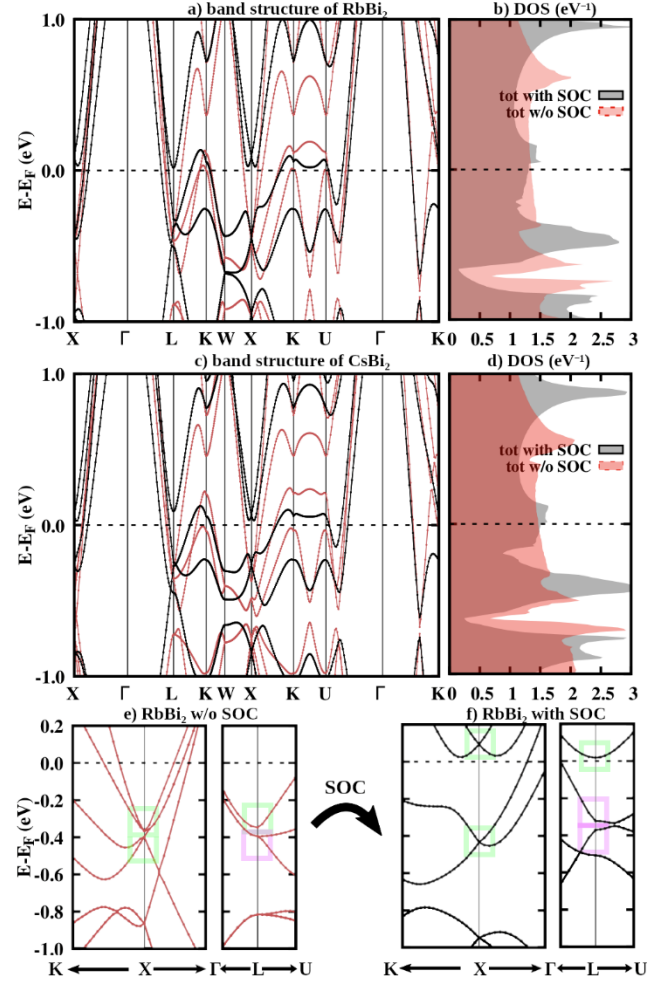


Fig. 6. Electronic band structure (a, c) and DOS (b, d) of RbBi<sub>2</sub> and CsBi<sub>2</sub> respectively, calculated in a scalar- (without SOC; red line) and fully relativistic approach (with SOC; black). Panels (e) and (f) show the band structure around the Brillouin zone center ( $\Gamma$ ) for RbBi<sub>2</sub>. At the  $X$  point the degeneracy is symmetry-protected, so the inclusion of SOC results only in shifting the band energies (points marked with green rectangles), while at  $L$ -point they are additionally split (purple rectangles).

In Figure 6 the scalar and fully-relativistic band structure is shown in a narrow energy range around  $E_F$ . In the case of RbBi<sub>2</sub>, when SOC not included, the Fermi level is positioned in the flat part of DOS, while with SOC the local maximum appears and Fermi level is situated on its slope.

The parabolic bands around  $\Gamma$  point with a large (3 eV) energy gap around the Fermi level are not affected by SOC. At many points of  $k$ -space (for example between  $K$  and  $U$  or  $X$  and  $\Gamma$  points), mainly below the Fermi level, the band crossings are removed by SOC.

Figure 7 shows the Fermi surface (FS) of RbBi<sub>2</sub> and CsBi<sub>2</sub> calculated with and without SOC. Since the differences in FS between the two compounds are negligible, we will discuss the

RbBi<sub>2</sub> case only. The only difference between the two compounds lies in the Fermi velocity which is slightly smaller in the case of CsBi<sub>2</sub> in the [1 0 0] direction. This is consistent with a less dispersed character of bands around E<sub>F</sub> and a higher DOS at the Fermi level of this compound.

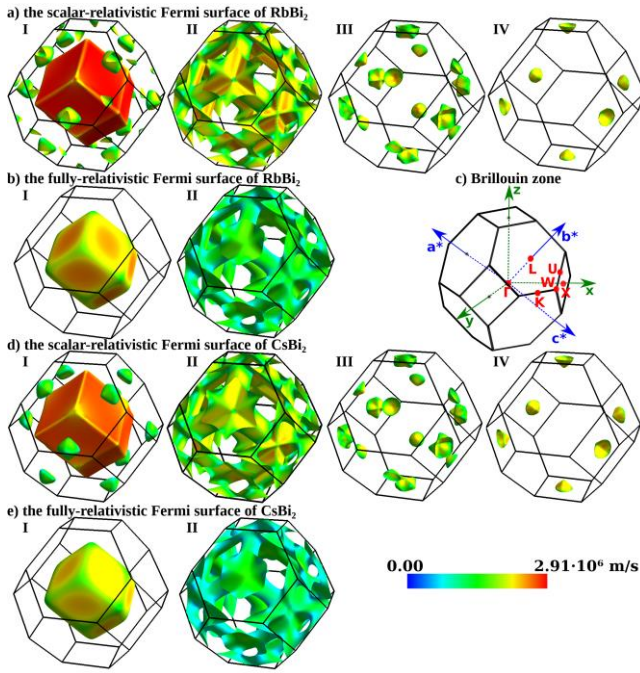


Fig. 7. Fermi surface of RbBi<sub>2</sub> (a, b) and CsBi<sub>2</sub> (d, e) calculated without SOC (a, d) and with SOC (b, e), colored according to Fermi velocity. The Brillouin zone with high symmetry points is shown in panel (c).

In the scalar relativistic case there are four bands per spin crossing the E<sub>F</sub>, and thus four FS branches. First one has a dodecahedral shape with almost completely flat faces. It is similar to the Fermi surface of Polonium which was concluded to lead to strong nesting, as one *q*-vector (connecting two flat faces) is able to connect many points of these faces of the Fermi surface, leading to the Kohn anomaly in phonon spectrum<sup>50-52</sup>. The hybridization causes the presence of cone-like corners, which at E = 0.35 eV below the E<sub>F</sub> are visible as Dirac-like bands at the *L* point. Additionally, there are small pockets around *K* and *U* points. This part of Fermi surface is associated with the band which is approximately parabolic around the  $\Gamma$  point and is contributing to Dirac-like cones at other points.

The second branch contains many cylinders and is associated with a flat band at the *K-U* line. The third and fourth branch of Fermi surface consist of pockets centered at *X* and *L* points.

At the *X* point all four bands are degenerate to two points, both ca. 0.5 eV below the Fermi level. The SOC shifts them leaving one below and one above the E<sub>F</sub>. This reduces the Fermi surface to just two branches: the dodecahedral and the cylindrical one, both centered at  $\Gamma$ .

The degeneracy of bands at *X*-point is symmetry-enforced and leads RbBi<sub>2</sub> and CsBi<sub>2</sub> to be classified topologically as ESFD (enforced semimetals with Fermi degeneracy), i.e. it is a material, which could be driven to a topological insulator state by symmetry breaking<sup>53</sup>. In contrast to the behavior at the *X* point, at *L* the bands are not only shifted (one of them is shifted above the Fermi level), but also split.

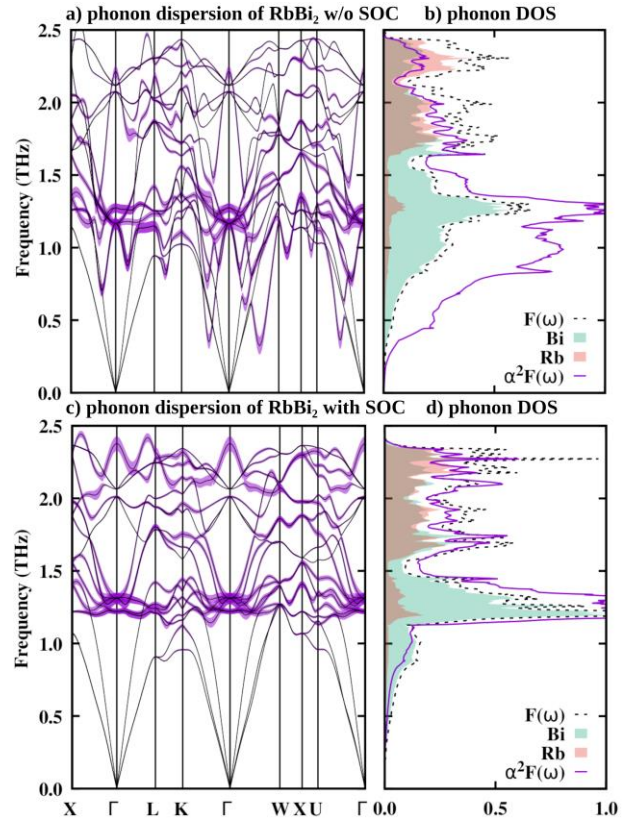


Fig. 8. Panels (a, c): Phonon dispersion relation of RbBi<sub>2</sub> with phonon linewidth proportional to the thickness of the purple line. Panels (b,d) show the phonon DOS (dashed black line) with atomic contribution marked in green (Bi) and red (Rb) and the Eliashberg function (purple line) normalized to 3N (N being a number of atoms per unit cell), calculated without SOC (a, b) and with SOC (c, d).

Despite the vanishing FS pockets, the DOS(E<sub>F</sub>) of RbBi<sub>2</sub> is almost unchanged by SOC (a negligible decrease from 1.35 to 1.31 eV<sup>-1</sup>/f.u. is seen). The reduction of the number of FS branches is compensated by the reduction of the Fermi velocity (see Fig. 9a-b), as lower velocity leads to a higher density of states.

Phonon structures of RbBi<sub>2</sub> and CsBi<sub>2</sub> are shown in Fig. 8 and 9. In contrast to the electronic structure, the phonon dispersion curves (Fig. 8 (a,c) and Fig. 9 (a,c)) and density of states (Fig. 8 (b,d) and Fig. 9 (b,d)) of the two compounds differ significantly.

The SOC has a major influence on phonons. When it is not taken into account, the vibrational structure of RbBi<sub>2</sub> is rich in softened modes, suggesting the instability of the structure. When SOC is included, the softening of modes disappears, indicating a stabilization by relativistic effects.

The phonon spectrum contains 18 modes, as the primitive cell of RbBi<sub>2</sub> contains 6 atoms (2 formula units). Phonon modes coming from Bi and Rb atomic vibrations are not strongly separated from each other as it is e.g. in the case of LiBi<sup>4</sup> or CaBi<sub>2</sub><sup>10</sup>. Three acoustic modes and low-frequency optic modes (up to  $\omega = 1.7$  THz) are mainly associated with Bi atoms vibrations, while high-frequency modes (in the range  $\omega = 1.7-2.5$  THz) come from Rb. Transverse acoustic (*TA*) modes are degenerate along the  $X-\Gamma-L$  path and split in the *xy* plane along  $W-\Gamma-K$ . The optical modes coming from Bi lie within a narrow frequency range  $\omega = 1.1$  to 1.4 THz and a part of them is almost

flat, resulting in a peak in the phonon DOS. The exception is the highest mode, which is the breathing mode of a pyrochlore network<sup>54-57</sup> associated with a movement of Bi atoms toward the center of the tetrahedron and breaking of the inversion symmetry of the lattice (see Fig. 9(e)).

The vibrations of atoms along the line, as in case of this mode is only a special case of trajectory of atoms, generally described by formula:

$$\mathbf{r}_s(t) = \text{Re}(\widehat{\epsilon}_{\nu s} \exp(i(\mathbf{q} \cdot \mathbf{R} - \omega_\nu t))) = \text{Re}(\widehat{\epsilon}_{\nu s}) \cdot \cos(\omega_\nu t + \mathbf{q} \cdot \mathbf{R}) + \text{Im}(\widehat{\epsilon}_{\nu s}) \cdot \sin(\omega_\nu t + \mathbf{q} \cdot \mathbf{R})$$

where  $\mathbf{r}_s(t)$  is position of atom  $s$  in time  $t$ , with crystallographic position  $\mathbf{R}$ ,  $\nu_s$  is its polarization vector associated with phonon mode  $\nu$  with frequency  $\omega_\nu$  and all is considered in the  $\mathbf{q}$ -point of the space of wave vectors.

With one of the part (real or imaginary) of polarization vector equal to zero, atoms vibrate along the line with frequency  $\omega$  and direction given by the polarization vector. When both parts are non-zero, the atomic trajectory is an ellipsoid. If additionally both parts are equal, the ellipsoid becomes a circle. Such a case has been found in many  $q$  points of phonon dispersion of RbBi<sub>2</sub>. Two examples are shown in Fig. 8(f-g). At the K point, Rb atoms are moving circularly, while Bi atoms move along a line. At the W point, all atoms are moving along a circle/ellipse. These modes might be candidates for chiral phonons which arise due to symmetry of the crystal structure and have been recently found in ABi compounds, including RbBi and CsBi<sup>58</sup> (the occurrence of chiral phonons in ABi<sub>2</sub> compounds is discussed in more detail in ref.<sup>59</sup>).

The phonon spectrum of CsBi<sub>2</sub> is qualitatively different from RbBi<sub>2</sub>. When SOC is neglected, the modes are not only softened as it is in the case of RbBi<sub>2</sub>, but the spectrum is rich in imaginary frequencies, suggesting structural instability. Inclusion of the SOC removes the imaginary frequencies, thus the relativistic effect of SOC is crucial for the stability of the cubic Laves structure of CsBi<sub>2</sub>.

As visualized in Fig. 9(e), the soft mode is associated with a movement of Bi atoms toward the center of faces of tetrahedron. As is highlighted in the electronic charge density plot (Fig. 4(b)), this point is characterized by large electronic charge density associated with metallic bonds of close-packed Bi tetrahedron. Thus this mode may be seen as movement of Bi ions, which are attracted to electronic charge, leading to lowering of frequency.

When SOC is included, the electronic structure changes and Bi atoms move in different direction and the imaginary frequencies disappear. As we checked, similar change of displacement vectors of atoms is associated with the disappearance of softened modes of RbBi<sub>2</sub>. This behavior may suggest that the softening arises from a Kohn anomaly caused by an electronic effect of nesting of the Fermi surface, which would be an interesting matter of further studies.

The influence of electronic surrounding on phonons is highlighted by large phonon linewidth of discussed modes, shown in Fig. 8(a) and Fig. 9(a) in a fat band representation. It is defined as

$$\gamma_{qv} = 2\pi\omega_{qv} \sum_{ij} \frac{d^3k}{\Omega_{BZ}} |g_{qv}(\mathbf{k}, i, j)|^2 \times \delta(E_{kj} - E_F) \delta(E_{k+q,i} - E_F)$$

Where electron-phonon coupling matrix element

$$g_{qv}(\mathbf{k}, i, j) = \sum_s \sqrt{\frac{\hbar}{2M_s\omega_{qv}}} \left\langle \psi_{i,\mathbf{k}+\mathbf{q}} \left| \frac{dV_{SCF}}{d\hat{u}_{\nu s}} \cdot \hat{\epsilon}_{\nu s} \right| \psi_{j\mathbf{k}} \right\rangle$$

describes how the electronic potential is changed by an atomic displacement,  $\omega_{qv}$  is a frequency of  $\nu$ -th mode with a wave vector  $\mathbf{q}$  (equal to a difference of wave vectors of two electronic states  $\psi_{i,\mathbf{k}+\mathbf{q}}, \psi_{j\mathbf{k}}$ ) with a polarization vector  $\hat{\epsilon}_{\nu s}$ , associated with a displacement  $\hat{u}_{\nu s}$  of  $s$ -th atom of a mass  $M_s$ . Dirac delta functions ensure that only the electronic states near the FS are included in calculation.

On the other hand, the EPC matrix influences the electron-phonon part of dynamical matrix, given by<sup>60</sup>

$$\Phi^{EP}(\mathbf{q})_{\kappa\alpha\kappa'\alpha'} = \frac{2}{N} \sum_{nn'k} \frac{f_{k+q,n} - f_{k,n}}{E_{k+q,n'} - E_{k,n}} (g_{qv}(k, i, j))^{\kappa\alpha} g_{qv}(k, i, j)^{\kappa'\alpha'}$$

where  $E_{k,n}$  and  $f_{k,n}$  are energy and occupancy of the  $n$ -th band at  $k$ -th point,  $N$  is a number of unit cells. The phonon frequencies are the eigenvalues of the dynamical matrix normalized by atomic masses. In consequence, the higher value of the EPC matrix leads to lower frequency. As a consequence, the phonon softening and phonon linewidth are associated with each other, as both depend on the EPC matrix and geometry of FS. It is visible in Fig. 8(a) and 9(a), where the softened modes are characterized by large phonon linewidth.

It is worth noting that not all softened modes disappeared with SOC. Many of softened optical modes survived and their large phonon linewidth demonstrates their importance for EPC and thus for superconductivity.

The influence of SOC on ABi<sub>2</sub> family is similar to the case of other family of Bi-rich superconductors, ABi<sub>3</sub>, which crystallize in a simple cubic AuCu<sub>3</sub>-type structure, within which the all A-Bi and Bi-Bi distances are equal. In case of lighter SrBi<sub>3</sub> the SOC only removes softened modes with large phonon linewidth, while in case of heavier BaBi<sub>3</sub> it also stabilizes the structure. In addition, both Ba- and Bi-derived modes of BaBi<sub>3</sub> are lower than in the case of SrBi<sub>3</sub>, leading to nearly 30% larger value of EPC constant, which is equal to 1.43 and 1.11 respectively<sup>12</sup>. In the ABi<sub>2</sub> family the substitution of lighter Rb with heavier Cs leads to only about 10% larger EPC constant.

Modes associated with Cs atoms have lower frequency than those associated with Rb (average frequency of Cs is 9% lower than that of Rb, see Table 2). This is expected since Cs is over 55% heavier than Rb. The average frequency of Bi is of 5% lower in CsBi<sub>2</sub> than in RbBi<sub>2</sub>. Surprisingly, not all modes of Bi are lowered leading to a completely different shape of phonon DOS, where the peak around 1.3 THz is spread out.

In order to better describe the difference between the phonon structures of CsBi<sub>2</sub> and RbBi<sub>2</sub>, dispersion relations around the  $\Gamma$  point are plotted and the modes associated with similar movement of atoms are marked with the same color in Fig. S3 of the Supplementary Material. Additionally, modes associated with the movement of Bi atoms are visualized in Fig. S3(c-f) of the Supplementary Material and force constants between atoms are shown in Fig. S3(g). The modes associated with a movement of both Bi (along Bi-Bi bonding) and Cs/Rb (Fig. S3(d)) are lowered from 1.31 in case of RbBi<sub>2</sub> to 1.03 THz in CsBi<sub>2</sub>, while the frequency of modes associated with a movement of Bi towards the empty space around Cs/Rb (Fig. S3(c,e)) are increased from 1.22 THz and 1.32 THz in RbBi<sub>2</sub> to 1.36 THz in CsBi<sub>2</sub>.

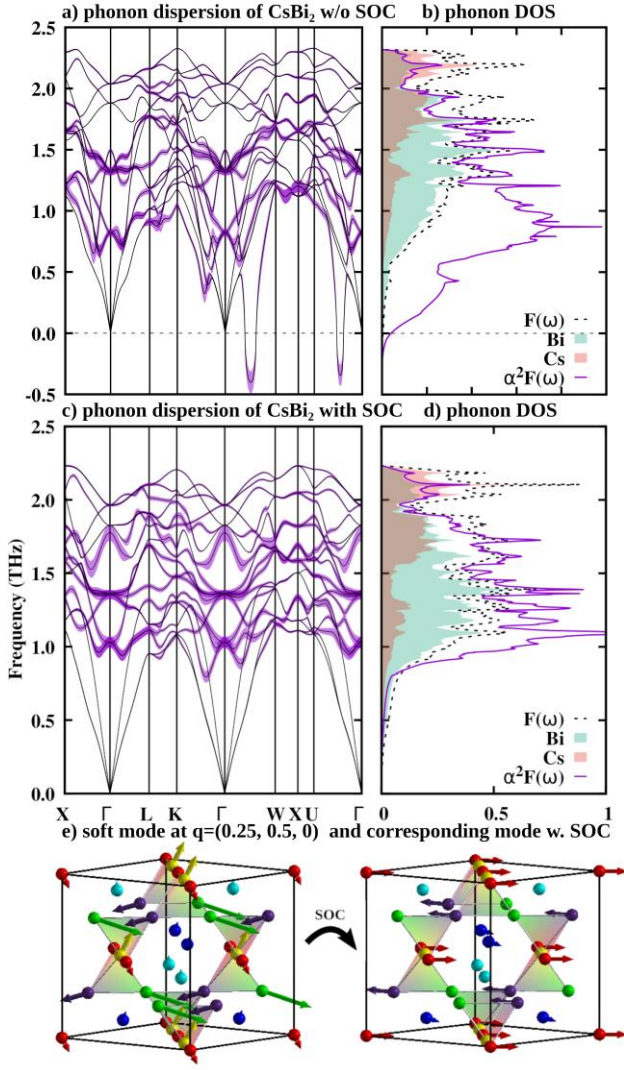


Fig. 9. Phonon dispersion relation of CsBi<sub>2</sub> together with phonon linewidth (a, c) and its phonon DOS together with atomic contribution to phonon DOS and Eliashberg function, calculated w/o SOC (a, b) and with SOC (c, d). The color scheme is the same as in Fig. 8. The soft mode, which appears along  $\Gamma$ – $W$  in the scalar relativistic case, is marked in real space with arrows (yellow, red, green, and purple spheres are Bi, light and dark blue are Cs).

In both compounds the phonon linewidths are large only in case of Bi modes. Since the FS is also dominated by  $6p$ -states of Bi, the superconductivity in ABi<sub>2</sub> is driven by the Bi pyrochlore lattice, as the electron-phonon coupling in both electronic and phonon ways is almost exclusively contributed by Bi.

This may be caused by a difference in the unit cell size, which is larger in the case of CsBi<sub>2</sub>, thus the Bi-Bi metallic bonding is slightly weaker leading to smaller force constants of Bi-Bi pairs (see Fig. S4(h) of the Supplementary Material) and lower frequencies of modes associated with a movement of Bi along Bi-Bi bonds. For the same reason, the highest optical mode associated with a movement of Bi toward the center of tetrahedron (Fig. S4(f)) is lowered from 2.37 THz in case of RbBi<sub>2</sub> to 1.78 THz in CsBi<sub>2</sub>. It is similar to the case of soft mode shown in Fig. 10(e) and explains why the effect of softening is stronger in case of CsBi<sub>2</sub>. On the other hand, the force constants of Bi-

Cs pairs are larger than of Bi-Rb pairs, leading to a higher frequencies of modes associated with a movements of Bi toward the space around Cs. These changes show that the substitution of Rb by Cs not only lowers the frequency due to a larger mass, but also influences the size of the unit cell and modifies the bonding of Bi network.

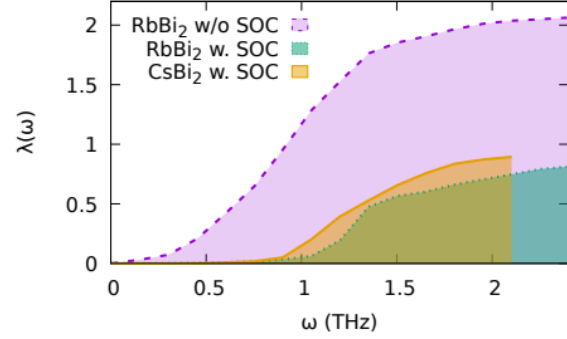


Fig. 10. The cumulative EPC constant of RbBi<sub>2</sub> and CsBi<sub>2</sub>.

On the basis of the phonon linewidth the Eliashberg function is calculated:

$$\alpha^2 F(\omega) = \frac{1}{2\pi N(E_F)} \sum_{qv} \delta(\omega - \omega_{qv}) \frac{\gamma_{qv}}{\hbar\omega_{qv}}$$

The Eliashberg function is effectively the phonon DOS weighted by a phonon linewidth divided by phonon energy and density of electronic states at Fermi level.

Eliashberg function of RbBi<sub>2</sub>, calculated without SOC, is the highest at low frequencies (up to 1.5 THz) due to the presence of softened acoustic modes and low-frequency optical modes. When SOC is included, the Eliashberg function becomes similar to phonon DOS, which means that electron-phonon coupling only weakly depends on phonon frequency. The largest contribution to Eliashberg function comes from highly-degenerate and partially flat Bi modes in the narrow frequency range.

**Table 2. The summary of calculated properties of RbBi<sub>2</sub> and CsBi<sub>2</sub> compared to experimental results (marked with label *expt.*). The density of states is given in units of  $eV^{-1}/f.u.$ , both mean frequency  $\bar{\omega}$  and logarithmic frequency  $\omega_{ln}$  in units of THz and critical temperatures in K.**

	RbBi <sub>2</sub>		CsBi <sub>2</sub>	
	w/o SOC	w. SOC	w/o SOC	w. SOC
$N(E_F)/f.u.$	1.35	1.31	1.46	1.51
$\lambda_{expt}$	0.82		0.87	
$\lambda$	2.06	0.81	---	0.92
$\bar{\omega}$	1.59 Rb: 1.91 Bi: 1.36	1.61 Rb: 1.85 Bi: 1.45		1.51 Cs: 1.69 Bi: 1.38
$\omega_{ln}$	0.85	1.74		1.27
$T_c$	6.18	3.31	3.85	
$T_c(expt.)$	4.24		4.65	

Having the Eliashberg function, we can calculate the electron-phonon coupling constant

$$\lambda = 2 \int_0^{\omega_{\max}} \frac{\alpha^2 F(\omega)}{\omega} d\omega.$$

It is essentially proportional to phonon linewidth divided by frequency squared, thus the low frequency modes contribute more than higher ones. Obtained values are shown in Table 2. When SOC is not included, the EPC constant of RbBi<sub>2</sub>  $\lambda_{\text{ep}} = 2.06$ , is more than twice larger than the experimental value. The cumulative EPC constant shown in Fig. 10 clearly shows that such a high value is caused by softened modes, which are characterized by low frequency and large phonon linewidth. When SOC is included, the softening disappears and EPC constant drops to  $\lambda_{\text{ep}} = 0.81$  (in excellent agreement with experimental value  $\lambda_{\text{ep}} = 0.82$ ), and is mostly delivered by acoustic and optical Bi modes, as the phonon linewidth is. The calculated EPC constant of CsBi<sub>2</sub>  $\lambda_{\text{ep}} = 0.92$  is also in a good agreement with the experimental value  $\lambda_{\text{ep}} = 0.87$ . It is slightly larger than in case of RbBi<sub>2</sub> due to a shift of part of modes to lower frequencies and slight changes in band structure. The impact of the electronic structure on EPC can be measured using the integral:

$$I = \int_0^{\omega_{\max}} \alpha^2 F(\omega) \cdot \omega d\omega$$

Which does not depend on phonon frequency, as:

$$I = \frac{1}{N(E_F)} \sum_{i,j} \frac{d^3 k}{\Omega_{\text{BZ}}} \left| \sum_s \frac{1}{\sqrt{2M_s}} \langle \psi_{i,k+q} \left| \frac{dV_{\text{SCF}}}{d\mathbf{u}_{\text{vs}}} \right| \psi_{j,k} \right|^2 \cdot \delta(E_{ki} - E_F) \delta(E_{k+q,j} - E_F)$$

In a monoatomic case this integral corresponds to Hopfield parameter. The calculated value of the integral is 0.90 and 1.26 for RbBi<sub>2</sub> and CsBi<sub>2</sub>, respectively. This suggests that, in addition to the lowering of frequency, the slight changes of the electronic structure resulting in lowering the Fermi velocity and increased DOS( $E_F$ ) strengthen the EPC.

On the basis of calculated EPC constant the critical temperature can be calculated with help of Allen-Dynes equation

$$T_c = \omega_{\text{ln}} \exp\left(-\frac{1.04(1 + \lambda)}{\lambda - \mu^*(1 + 0.62\lambda)}\right)$$

where

$$\omega_{\text{ln}} = \exp\left(\frac{\int_0^{\omega_{\max}} \alpha^2 F(\omega) \ln(\omega) \frac{d\omega}{\omega}}{\int_0^{\omega_{\max}} \alpha^2 F(\omega) \frac{d\omega}{\omega}}\right)$$

is a logarithmic average of frequency. In the case of RbBi<sub>2</sub>  $\lambda = 0.81$  and  $\omega_{\text{ln}} = 1.74$  THz (equivalent to 83.5 K) leading to  $T_c = 3.23$  K, reasonably close to the measured value 4.24 K. In case of CsBi<sub>2</sub> EPC constant in larger ( $\lambda = 0.92$ ) leading to higher  $T_c = 3.85$  K despite of lower logarithmic frequency. The estimated critical temperature is reasonably close to the experimental value  $T_c = 4.65$  K. Both experimental and calculated values lead to a conclusion, that CsBi<sub>2</sub> has higher critical temperature than RbBi<sub>2</sub> due to slightly stronger electron-phonon coupling.

In summary, the structural arrangement of Bi atoms into a pyrochlore network of Bi tetrahedra intercalated with alkali metal atoms, results in a relatively high electron-phonon coupling

constant. This emerges as a combination of both aforementioned factors: the large electronic density within the close-packed Bi atoms in Bi<sub>4</sub> tetrahedra allows for the strong interaction of phonon modes with electrons (large phonon linewidths), whereas the tetrahedra themselves are relatively loosely packed within the unit cell with a large amount of “free space” filled only by Rb/Cs atoms. This, in combination with high atomic mass of Bi, results in relatively low Bi phonon frequencies, enhancing the EPC. Recently we discussed a similar situation in isostructural Laves phase superconductors: SrRh<sub>2</sub> and SrIr<sub>2</sub>, where the pyrochlore lattice or Rh/Ir was found to be responsible for the emergence of strong-coupling superconductivity.

On the other hand RbBi<sub>2</sub> and CsBi<sub>2</sub> are in contrast with CaBi<sub>2</sub>, which crystallizes in an orthorhombic structure that can be viewed in a distorted Laves phase structure, in which tetrahedrons are distorted to Bi-Bi and Ca-Bi planes separated from each other. Here the phonon linewidths are smaller and average Bi frequencies are higher, leading to the EPC constant  $\lambda_{\text{ep}} = 0.54$ , much lower than  $\lambda_{\text{ep}} = 0.82$  and  $\lambda_{\text{ep}} = 0.87$  for RbBi<sub>2</sub> and CsBi<sub>2</sub>, respectively, despite the value of  $I = 1.17$  lying between RbBi<sub>2</sub> and CsBi<sub>2</sub> cases. This results in a lower critical temperature ( $T_c = 2.0$  K for CaBi<sub>2</sub>)<sup>9,10</sup>. It is worth mentioning that the average Bi frequency in elemental Bi, the phonon structure of which is presented in Fig. S8 of the Supplementary Material and summarized in Table 2, is also higher than in the studied Laves phases. Since Bi is a semimetal, the DOS( $E_F$ ) and the value of  $I$  are small, leading to a low value of the EPC parameter  $\lambda_{\text{ep}} = 0.23$  and very low predicted critical temperature  $T_c = 0.7$  mK in a fair agreement with the experimental  $T_c = 5$  mK<sup>61</sup>.

Electron population analysis on RbBi<sub>2</sub> shows that the DOS( $E_F$ ) is contributed mostly by electrons occupying nearest-neighbor Bi-Bi antibonding states (see Fig. S4 of the Supplementary Material). A hypothetical neutral Bi pyrochlore lattice would have its  $E_F$  lying close to a pseudogap. The two electrons donated by Rb increase the antibonding population, destabilizing the lattice. Unfortunately, with the currently available computational tools (either direct in case of local basis set or indirect - via projection of plane-wave wavefunctions to a local orbitals set<sup>62-65</sup>) the bonding population analysis can only be performed in a scalar-relativistic case. While for bonding of lighter elements SR approximation is reasonably applicable, the chemical bonding in 6<sup>th</sup> and 7<sup>th</sup> period elements is heavily influenced by SOC effects<sup>66,67</sup>. A possible solution for reliable population analysis of compounds of the heaviest elements is via the localized Wannier spinors<sup>68</sup>.

The calculated electronic structure of the Bi<sub>4</sub> cluster (shown in Fig. 11) are in general consistent with the previous results by Lohr and Pyykkö obtained by means of relativistically-parametrized extended Hückel method<sup>69</sup>, although the ordering of virtual orbitals is slightly different. The stabilizing effect of SOC on ABi<sub>2</sub> can be qualitatively understood by considering the electronic structure of a  $T_d$  Bi<sub>4</sub> cluster. Firstly, in a heavy element, such as Bi scalar-relativistic effects result in a complete energetic separation of 6s and 6p orbitals<sup>48</sup>. Thus, only the p orbitals participate in the bonding. Secondly, the SOC splits the 6p atomic level into  $p_{1/2}$  and  $p_{3/2}$  separated by ca. 2 eV in a free atom. In the scalar-relativistic approximation the neutral Bi<sub>4</sub> cluster is a closed-shell system with four electrons occupying the doubly-degenerate  $e$  HOMO level. With 2 additional electrons donated by electropositive species, the Bi<sub>4</sub><sup>2-</sup> is first-order

Jahn-Teller (JT) active due to two electrons occupying a triply degenerate  $t_1$  level. SOC splits the  $6p$ -derived levels ( $6s$ -derived lower  $t_2$  level is also weakly split due to small admixture of the  $p$  character), lifting the triple degeneracy of  $t_1$  and  $t_2$ . The two additional electrons now occupy a  $e'$  ( $\Gamma_6$ ) level, quasi-degenerate ( $\Delta E \approx 0.02$  eV) with the next  $e''$  ( $\Gamma_7$ ) leading to structural stabilization. However, the splitting of the  $e'$  and the two  $u'$  ( $\Gamma_8$ ) levels is relatively small ( $\Delta E \approx 0.9$  and  $1.2$  eV, respectively), resulting in a possibility of a second-order JT instability, as pointed out by Lohr and Pyykkö<sup>69</sup>. While the electronic structure of the crystalline  $ABi_2$  compound is much more complex than of isolated cluster, the stabilizing effects of SOC similarly stem from the lifted  $p$  orbital degeneracy while the weakened but persistent mode softening can be considered an effect of a second-order JT (SOJT) effect.

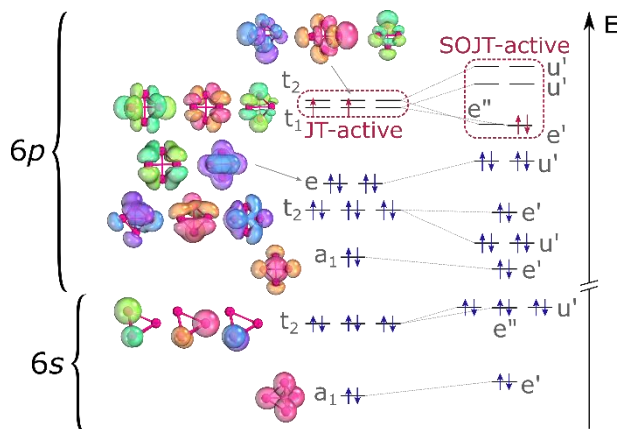


Fig. 11 Molecular orbitals of a tetrahedral  $Bi_4$  cluster. Note that for clarity of the picture the energy scale (right) is divided into two parts, as the separation between lower  $t_2$  and higher  $a_1$  levels is on the order of 8 eV, while for comparison the  $t_2$ - $e$  splitting is ca. 0.5 eV.

This observation suggest a criterion for finding new superconductors: one may look for compounds stabilized by strong SOC, which should show relatively strong electron-phonon coupling while avoiding crystal structure distortion.

Examples of such SOC stabilized superconductors can be found among Sb-, Bi- and Pb-rich intermetallic phases featuring hypervalent polyanions, listed in Table 3.

$KBi_2$ ,  $RbBi_2$ ,  $CsBi_2$  belong to a large family of cubic Laves (C-15) superconductors. The SuperCon database lists 192 C-15 superconductors, belonging to 16 different chemical systems, with critical temperatures ranging from 0.7 to 10.7 K. However, the three Bi-based compounds distinguish themselves from the whole family in a number of ways. Firstly, besides  $LaAl_2$  ( $T_c \approx 3$  K<sup>75</sup>) and  $LaMg_2$  ( $T_c \approx 1$  K), they are the only main-group element-based Laves superconductors. Secondly, we have shown that in  $RbBi_2$  and  $CsBi_2$  systems the superconductivity clearly emerges from the electron-rich Bi pyrochlore lattice, with Rb/Cs acting predominantly as electron donors to the Bi lattice. Such clear picture is not possible in case of transition metal based systems, where the bonding between atoms occupying the two crystal sites is expected to be much more metallic. Lastly, Bi is the heaviest stable element ( $Z = 83$ ) and the relativistic effects on electronic properties in  $KBi_2$ ,  $RbBi_2$ , and  $CsBi_2$  are the strongest of all of the Laves superconductors, even

when compared with Ir- and Au- based systems, such as  $(La/Lu)Ir_2$ <sup>76</sup> and  $(Pb,Bi)Au_2$ <sup>77</sup>, since the SOC effect on  $5d$  valence electrons is weaker than on  $6p$  shell.

**Table 3 Superconductors featuring Sb-, Te-, Bi-, and Pb-based hypervalent polyanions.**

Material	Hypervalent network	$T_c$
$Ba_3TiTe_5$	1d $Te^-$ chains	6 K ( $p = 37$ GPa) <sup>70</sup>
$YbSb_2$	2d $Sb^-$ square network	1.3 K <sup>45,71</sup>
$LiBi$	2d $Bi^-$ square network	2.5 K <sup>4,15</sup>
$NaBi$	2d $Bi^-$ square network	2.15 K <sup>3</sup>
$CaBi_2$	2d $Bi^-$ square network	2.0 K <sup>9</sup>
$Ba_2Bi(Bi_xSb_{1-x})_2$	2d $Sb/Bi$ "square-honeycomb"	max. 4.4 K <sup>14,72</sup>
$LaPb_3$	3d $Pb^-$ cubic network	4 K <sup>73</sup>
$LaBi_3$	3d $Bi^-$ cubic network	7.3 K <sup>74</sup>

## CONCLUSIONS

We have analyzed the electronic and vibrational properties of two Bi-based cubic Laves phases:  $RbBi_2$  and  $CsBi_2$ . Our results show that the occurrence of superconductivity in these two compounds and an isostructural  $KBi_2$  stems almost exclusively from the heavy element pyrochlore lattice. Both the stability of the phases and their electronic and vibrational properties are heavily affected by relativistic effects. The spin-orbit coupling is crucial for the dynamic stability of  $CsBi_2$ , and to a lesser extent  $RbBi_2$ . The stability enhancement can be explained by considering an isolated  $Bi_4$  cluster and the effects of SOC on its electronic structure. We postulate that crystal structures based on relativistically-stabilized hypervalent networks of heavy elements are interesting candidates for finding new superconductors.

## ASSOCIATED CONTENT

**Supporting Information.** PXRD patterns for  $RbBi_2$  and  $CsBi_2$  samples. Crystallographic unit cell parameters for  $RbBi_2$  and  $CsBi_2$ . Low temperature heat capacity. Details of phonon dispersion relations and visualization of Bi-associated modes. Crystal orbital Hamilton population (COHP) plot for  $RbBi_2$ . This material is available free of charge via the Internet at <http://pubs.acs.org>.

## AUTHOR INFORMATION

Corresponding Author

\* [michal.winiarski@pg.edu.pl](mailto:michal.winiarski@pg.edu.pl)

Author Contributions

The manuscript was written through contributions of all authors.

Funding Sources

The research performed at the AGH-UST was supported by the National Science Center (Poland), Project No. 2017/26/E/ST3/00119. S.G. was partly supported by the EU Project POWR.03.02.00-00-I004/16.

## ACKNOWLEDGMENT

We gratefully acknowledge helpful discussions with Dr. Andrzej Ptok (INP PAS, Poland)

## ABBREVIATIONS

DKH2 – Douglas-Kroll-Hess – second-order Douglas-Kroll-Hess relativistic correction, DOS – density of states, GGA – generalized gradient approximation, PBE – Perdew-Burke-Ernzerhof exchange-correlation potential, PXRD – powder x-ray diffraction, QE – Quantum Espresso package, SOC – spin-orbit coupling, EPC – electron-phonon coupling

## REFERENCES

- (1) Nesper, R. Structure and Chemical Bonding in Zintl-Phases Containing Lithium. *Prog. Solid State Chem.* **1990**, *20* (1), 1–45.
- (2) Papoian, G. A.; Hoffmann, R. Hypervalent Bonding in One, Two, and Three Dimensions: Extending the Zintl-Klemm Concept to Nonclassical Electron-Rich Networks. *Angew. Chem. Int. Ed.* **2000**, *39* (14), 2408–2448.
- (3) Kushwaha, S. K.; Krizan, J. W.; Xiong, J.; Klimczuk, T.; Gibson, Q. D.; Liang, T.; Ong, N. P.; Cava, R. J. Superconducting Properties and Electronic Structure of NaBi. *J. Phys.: Condens. Matter* **2014**, *26* (21), 212201.
- (4) Górnicka, K.; Gutowska, S.; Winiarski, M. J.; Wiendlocha, B.; Xie, W.; Cava, R. J.; Klimczuk, T. Superconductivity on a Bi Square Net in LiBi. *Chem. Mater.* **2020**, *32* (7), 3150–3159.
- (5) Merlo, F.; Fornasini, M. L. Crystal Structure of Some Phases and Alloying Behaviour in Alkaline Earths, Europium and Ytterbium Pnictides. *Mater. Res. Bull.* **1994**, *29* (2), 149–154.
- (6) Ovchinnikov, A.; Bobev, S. Bismuth as a Reactive Solvent in the Synthesis of Multicomponent Transition-Metal-Bearing Bismuthides. *Inorg. Chem.* **2020**, *59* (6), 3459–3470.
- (7) Tremel, W.; Hoffmann, R. Square Nets of Main-Group Elements in Solid-State Materials. *J. Am. Chem. Soc.* **1987**, *109* (1), 124–140.
- (8) Sturza, M.; Han, F.; Malliakas, C. D.; Chung, D. Y.; Claus, H.; Kanatzidis, M. G. Superconductivity in the Intermetallic Pnictide Compound Ca11Bi10. *Phys. Rev. B* **2014**, *89* (5), 054512.
- (9) Winiarski, M. J.; Wiendlocha, B.; Gołab, S.; Kushwaha, S. K.; Wiśniewski, P.; Kaczorowski, D.; Thompson, J. D.; Cava, R. J.; Klimczuk, T. Superconductivity in CaBi2. *Phys. Chem. Chem. Phys.* **2016**, *18* (31), 21737–21745.
- (10) Gołab, S.; Wiendlocha, B. Electron-Phonon Superconductivity in CaBi2 and the Role of Spin-Orbit Interaction. *Phys. Rev. B* **2019**, *99* (10), 104520.
- (11) Iyo, A.; Yanagi, Y.; Kinjo, T.; Nishio, T.; Hase, I.; Yanagisawa, T.; Ishida, S.; Kito, H.; Takeshita, N.; Oka, K. et al. Large Enhancement of Superconducting Transition Temperature of SrBi3 Induced by Na Substitution for Sr. *Sci. Rep.* **2015**, *5*, 10089.
- (12) Shao, D. F.; Luo, X.; Lu, W. J.; Hu, L.; Zhu, X. D.; Song, W. H.; Zhu, X. B.; Sun, Y. P. Spin-Orbit Coupling Enhanced Superconductivity in Bi-Rich Compounds ABi3 (A = Sr and Ba). *Sci. Rep.* **2016**, *6*, 21484.
- (13) Haldolaarachchige, N.; Kushwaha, S. K.; Gibson, Q.; Cava, R. J. Superconducting Properties of BaBi3. *Supercond. Sci. Technol.* **2014**, *27* (10), 105001.
- (14) Iyo, A.; Yanagi, Y.; Ishida, S.; Oka, K.; Yoshida, Y.; Kihou, K.; Lee, C. H.; Kito, H.; Takeshita, N.; Hase, I. et al. H. Superconductivity at 4.4 K in Ba 2 Bi 3. *Supercond. Sci. Technol.* **2014**, *27* (7), 072001.
- (15) Sambongi, T. Superconductivity of LiBi. *J. Phys. Soc. Jpn.* **1971**, *30* (1), 294–294.
- (16) Sun, S.; Liu, K.; Lei, H. Type-I Superconductivity in KBi2 Single Crystals. *J. Phys.: Condens. Matter* **2016**, *28* (8), 085701.
- (17) Li, H.; Wang, Y.; Aoki, Y.; Nishiyama, S.; Yang, X.; Taguchi, T.; Miura, A.; Suzuki, A.; Zhi, L.; Goto, H.; Eguchi, R. et al. A New Protocol for the Preparation of Superconducting KBi2. *RSC Adv.* **2020**, *10* (45), 26686–26692.
- (18) Li, H.; Ikeda, M.; Suzuki, A.; Taguchi, T.; Zhang, Y.; Goto, H.; Eguchi, R.; Liao, Y.-F.; Ishii, H.; Kubozono, Y. Pressure Dependence of Superconductivity in Alkali-Bi Compounds KBi2 and RbBi2. *Phys. Chem. Chem. Phys.* **2022**.
- (19) Roberts, B. W. Survey of Superconductive Materials and Critical Evaluation of Selected Properties. *J. Phys. Chem. Ref. Data* **1976**, *5* (3), 581–822.
- (20) Dshemuchadse, J.; Steurer, W. Some Statistics on Intermetallic Compounds. *Inorg. Chem.* **2015**, *54* (3), 1120–1128.
- (21) Xiao-Wu, L.; Hui-Ping, Y. C.-Y. Z. MgIn2: Synthesis, Crystal and Band Structure. *Chin. J. Inorg. Chem.* **2012**, *28* (4), 795–800.
- (22) Liu, X.; Zhao, H.; Kulka, A.; Tenczek-Zajac, A.; Xie, J.; Chen, N.; Świerczek, K. Characterization of the Physicochemical Properties of Novel SnS2 with Cubic Structure and Diamond-like Sn Sublattice. *Acta Mater.* **2015**, *82*, 212–223.
- (23) Le Bail, A. Whole Powder Pattern Decomposition Methods and Applications: A Retrospection. *Powder Diffr.* **2005**, *20* (04), 316–326.
- (24) Rodríguez-Carvajal, J. Recent Advances in Magnetic Structure Determination by Neutron Powder Diffraction. *Physica B: Condensed Matter* **1993**, *192* (1), 55–69.
- (25) Giannozzi, P.; Baroni, S.; Bonini, N.; Calandra, M.; Car, R.; Cavazzoni, C.; Davide Ceresoli; Chiarotti, G. L.; Cococcioni, M.; Dabo, I. et al. QUANTUM ESPRESSO: A Modular and Open-Source Software Project for Quantum Simulations of Materials. *J. Phys.: Condens. Matter* **2009**, *21* (39), 395502.
- (26) Perdew, J. P.; Burke, K.; Ernzerhof, M. Generalized Gradient Approximation Made Simple. *Phys. Rev. Lett.* **1996**, *77* (18), 3865–3868.
- (27) Kucukbenli, E.; Monni, M.; Adetunji, B. I.; Ge, X.; Adebayo, G. A.; Marzari, N.; de Gironcoli, S.; Dal Corso, A. Projector Augmented-Wave and All-Electron Calculations across the Periodic Table: A Comparison of Structural and Energetic Properties. *arXiv.org (Condensed Matter, Materials Science)*, April 11, 2014, 1404.3015, Ver. 1, <https://arxiv.org/abs/1404.3015>
- (28) Dronskowski, R.; Bloechl, P. E. Crystal Orbital Hamilton Populations (COHP): Energy-Resolved Visualization of Chemical Bonding in Solids Based on Density-Functional Calculations. *J. Phys. Chem.* **1993**, *97* (33), 8617–8624.
- (29) Steinberg, S.; Dronskowski, R. The Crystal Orbital Hamilton Population (COHP) Method as a Tool to Visualize and Analyze Chemical Bonding in Intermetallic Compounds. *Crystals* **2018**, *8* (5), 225.
- (30) *The STUTTGART TB-LMTO-ASA program.* <https://www2.fkf.mpg.de/andersen/LMTODOC/LMTODOC.html>.
- (31) Skriver, H. L. *The LMTO Method: Muffin-Tin Orbitals and Electronic Structure*; Springer-Verlag: Berlin; New York, 1984.
- (32) Perdew, J. P.; Wang, Y. Accurate and Simple Analytic Representation of the Electron-Gas Correlation Energy. *Phys. Rev. B* **1992**, *45* (23), 13244–13249.
- (33) Repisky, M.; Komorovsky, S.; Kadek, M.; Konecny, L.; Ekström, U.; Malkin, E.; Kaupp, M.; Ruud, K.; Malkina, O. L.; Malkin, V. G. ReSpec: Relativistic Spectroscopy DFT Program Package. *J. Chem. Phys.* **2020**, *152* (18), 184101.
- (34) Dyall, K. G. Relativistic Quadruple-Zeta and Revised Triple-Zeta and Double-Zeta Basis Sets for the 4p, 5p, and 6p Elements. *Theor. Chem. Acc.* **2006**, *115* (5), 441–447.
- (35) Knizia, G.; Klein, J. E. M. N. Electron Flow in Reaction Mechanisms—Revealed from First Principles. *Angew. Chem. Int. Ed.* **2015**, *54* (18), 5518–5522.
- (36) *IboView* [http://www.iboview.org/\\_bgBqyRo.html](http://www.iboview.org/_bgBqyRo.html)
- (37) Gnutzmann, G.; Dorn, F. W.; Klemm, W. Das Verhalten der Alkalimetalle zu Halbmetallen. VII. Über einige A3B- und AB2-Verbindungen der schweren Alkalimetalle mit Elementen der V. Gruppe. *Z. Anorg. Allgem. Chem.* **1961**, *309* (3–4), 210–225.
- (38) Emmerling, F.; Längin, N.; Petri, D.; Kroeker, M.; Röhr, C. Alkalimetallbismutide ABi und ABi2 (A = K, Rb, Cs) — Synthesen, Kristallstrukturen, Eigenschaften. *Z. Anorg. Allgem. Chem.* **2004**, *630* (1), 171–178.
- (39) Kelly, F. M.; Pearson, W. B. The Rubidium Transition at ~180°K. *Can. J. Phys.* **1955**, *33* (1), 17–24.

- (40) Weir, C. E.; Piermarini, G. J.; Block, S. On the Crystal Structures of Cs II and Ga II. *J. Chem. Phys.* **1971**, *54* (6), 2768–2770.
- (41) Cucka, P.; Barrett, C. S. The Crystal Structure of Bi and of Solid Solutions of Pb, Sn, Sb and Te in Bi. *Acta Cryst* **1962**, *15* (9), 865–872.
- (42) Lynton, E. A. *Superconductivity*; Chapman and Hall, 1971.
- (43) Powell, R. L.; Clark, A. F. Definitions of Terms for Practical Superconductors. 2. Critical Parameters. *Cryogenics* **1978**, *18* (3), 137–141.
- (44) Svanidze, E.; Morosan, E. Type-I Superconductivity in ScGa<sub>3</sub> and LuGa<sub>3</sub> Single Crystals. *Phys. Rev. B* **2012**, *85* (17), 174514.
- (45) Zhao, L. L.; Lausberg, S.; Kim, H.; Tanatar, M. A.; Brando, M.; Prozorov, R.; Morosan, E. Type-I Superconductivity in YbSb<sub>2</sub> Single Crystals. *Phys. Rev. B* **2012**, *85* (21), 214526.
- (46) Peets, D. C.; Cheng, E.; Ying, T.; Kriener, M.; Shen, X.; Li, S.; Feng, D. Type-I Superconductivity in Al<sub>6</sub>Re. *Phys. Rev. B* **2019**, *99* (14), 144519.
- (47) Górnicka, K.; Kuderowicz, G.; Carnicom, E. M.; Kutorasiński, K.; Wiendlocha, B.; Cava, R. J.; Klimczuk, T. Soft-Mode Enhanced Type-I Superconductivity in LiPd<sub>2</sub>Ge. *Phys. Rev. B* **2020**, *102* (2), 024507.
- (48) Pyykkö, P. Relativistic Effects in Chemistry: More Common Than You Thought. *Annu. Rev. Phys. Chem.* **2012**, *63* (1), 45–64.
- (49) Li, Y.; Wang, E.; Zhu, X.; Wen, H.-H. Pressure-Induced Superconductivity in Bi Single Crystals. *Phys. Rev. B* **2017**, *95* (2), 024510.
- (50) Kang, C.-J.; Kim, K.; Min, B. I. Phonon Softening and Superconductivity Triggered by Spin-Orbit Coupling in Simple-Cubic alpha-Polonium Crystals. *Phys. Rev. B* **2012**, *86* (5), 054115.
- (51) Min, B. I.; Shim, J. H.; Park, M. S.; Kim, K.; Kwon, S. K.; Yoon, S. J. Origin of the Stabilized Simple-Cubic Structure in Polonium: Spin-Orbit Interaction versus Peierls Instability. *Phys. Rev. B* **2006**, *73* (13), 132102.
- (52) Verstraete, M. J. Phases of Polonium via Density Functional Theory. *Phys. Rev. Lett.* **2010**, *104* (3), 035501.
- (53) Bradlyn, B.; Elcoro, L.; Cano, J.; Vergniory, M. G.; Wang, Z.; Felsner, C.; Aroyo, M. I.; Bernevig, B. A. Topological Quantum Chemistry. *Nature* **2017**, *547* (7663), 298–305.
- (54) Engelkemier, J.; Fredrickson, D. C. Chemical Pressure Schemes for the Prediction of Soft Phonon Modes: A Chemist's Guide to the Vibrations of Solid State Materials. *Chem. Mater.* **2016**, *28* (9), 3171–3183.
- (55) Schuck, G.; Kazakov, S. M.; Rogacki, K.; Zhigadlo, N. D.; Karpinski, J. Crystal Growth, Structure, and Superconducting Properties of the beta-Pyrochlore KOs<sub>2</sub>O<sub>6</sub>. *Phys. Rev. B* **2006**, *73* (14), 144506.
- (56) Bzdušek, T.; Rüegg, A.; Sigrist, M. Weyl Semimetal from Spontaneous Inversion Symmetry Breaking in Pyrochlore Oxides. *Phys. Rev. B* **2015**, *91* (16), 165105.
- (57) Gutowska, S.; Górnicka, K.; Wójcik, P.; Klimczuk, T.; Wiendlocha, B. Strong-Coupling Superconductivity of SrIr<sub>2</sub> and SrRh<sub>2</sub>: Phonon Engineering of Metallic Ir and Rh. *Phys. Rev. B* **2021**, *104* (5), 054505.
- (58) Skórka, J.; Kapcia, K. J.; Jochym, P. T.; Ptok, A. Chiral Phonons in Binary Compounds ABi (A = K, Rb, Cs) with P21/c Structure. *arXiv.org (Condensed Matter, Materials Science)*, March 10, 2022, 2203.05524, ver. 1, <https://arxiv.org/abs/2203.05524>.
- (59) Surajit Basak, Przemysław Piekarz, Andrzej Ptok, Chiral phonon in the cubic system based on the Laves phase of ABi<sub>2</sub> (A = K, Rb, Cs) (2022), *submitted*
- (60) Heid, R.; Pintschovius, L.; Reichardt, W.; Bohnen, K.-P. Anomalous Lattice Dynamics of Ruthenium. *Phys. Rev. B* **2000**, *61* (18), 12059–12062.
- (61) Prakash, O.; Kumar, A.; Thamizhavel, A.; Ramakrishnan, S. Evidence for Bulk Superconductivity in Pure Bismuth Single Crystals at Ambient Pressure. *Science* **2017**, *355* (6320), 52–55.
- (62) Maintz, S.; Deringer, V. L.; Tchougréeff, A. L.; Dronskowski, R. Analytic Projection from Plane-Wave and PAW Wavefunctions and Application to Chemical-Bonding Analysis in Solids. *J. Comput. Chem.* **2013**, *34* (29), 2557–2567.
- (63) Maintz, S.; Deringer, V. L.; Tchougréeff, A. L.; Dronskowski, R. LOBSTER: A Tool to Extract Chemical Bonding from Plane-Wave Based DFT. *J. Comput. Chem.* **2016**, *37* (11), 1030–1035.
- (64) Segall, M. D.; Shah, R.; Pickard, C. J.; Payne, M. C. Population Analysis of Plane-Wave Electronic Structure Calculations of Bulk Materials. *Phys. Rev. B* **1996**, *54* (23), 16317–16320.
- (65) Dunnington, B. D.; Schmidt, J. R. Generalization of Natural Bond Orbital Analysis to Periodic Systems: Applications to Solids and Surfaces via Plane-Wave Density Functional Theory. *J. Chem. Theory Comput.* **2012**, *8* (6), 1902–1911.
- (66) Pitzer, K. S. Relativistic Effects on Chemical Properties. *Acc. Chem. Res.* **1979**, *12* (8), 271–276.
- (67) Ziegler, T.; Snijders, J. G.; Baerends, E. J. Relativistic Effects on Bonding. *J. Chem. Phys.* **1981**, *74* (2), 1271–1284.
- (68) Kundu, S.; Bhattacharjee, S.; Lee, S.-C.; Jain, M. Population Analysis with Wannier Orbitals. *J. Chem. Phys.* **2021**, *154*, 104111.
- (69) Lohr, L. L.; Pyykkö, P. Relativistically Parameterized Extended Hückel Theory. *Chem. Phys. Lett.* **1979**, *62* (2), 333–338.
- (70) Zhang, J.; Jia, Y.; Wang, X.; Li, Z.; Duan, L.; Li, W.; Zhao, J.; Cao, L.; Dai, G.; Deng, Z. et al. A New Quasi-One-Dimensional Compound Ba<sub>3</sub>TiTe<sub>5</sub> and Superconductivity Induced by Pressure. *NPG Asia Mater.* **2019**, *11* (1), 60. <https://doi.org/10.1038/s41427-019-0158-2>.
- (71) Yamaguchi, Y.; Waki, S.; Mitsugi, K. Superconductivity of YbSb<sub>2</sub>. *J. Phys. Soc. Jpn.* **1987**, *56* (1), 419–420.
- (72) Yajima, T.; Takeiri, F.; Nozaki, Y.; Li, Z.; Tohyama, T.; Green, M. A.; Kobayashi, Y.; Kageyama, H. Superconductivity in the Hypervalent Compound Ba<sub>2</sub>Bi(Sb<sub>1-x</sub>Bi<sub>x</sub>)<sub>2</sub> with a Square-Honeycomb Lattice. *J. Phys. Soc. Jpn.* **2014**, *83* (7), 073705.
- (73) Havinga, E. E.; Damsma, H.; Van Maaren, M. H. Oscillatory Dependence of Superconductive Critical Temperature on Number of Valency Electrons in Cu<sub>3</sub>Au-Type Alloys. *J. Phys. Chem. Sol* **1970**, *31* (12), 2653–2662.
- (74) Kinjo, T.; Kajino, S.; Nishio, T.; Kawashima, K.; Yanagi, Y.; Hase, I.; Yanagisawa, T.; Ishida, S.; Kito, H.; Takeshita, N. et al. Superconductivity in LaBi<sub>3</sub> with AuCu<sub>3</sub>-Type Structure. *Supercond. Sci. Technol.* **2016**, *29* (3), 03LT02.
- (75) Pepperl, G.; Umlauf, E.; Meyer, A.; Keller, J. The Influence of Crystal Field Split Impurities (Tb) on the Superconducting Properties of LaAl<sub>2</sub>. *Solid State Commun.* **1974**, *14* (2), 161–165.
- (76) Geballe, T. H.; Matthias, B. T.; Compton, V. B.; Corenzwit, E.; Hull, G. W.; Longinotti, L. D. Superconductivity in Binary Alloy Systems of the Rare Earths and of Thorium with Pt-Group Metals. *Phys. Rev.* **1965**, *137* (1A), A119–A127.
- (77) Chen, K. W.; Graf, D.; Besara, T.; Gallagher, A.; Kikugawa, N.; Balicas, L.; Siegrist, T.; Shekhter, A.; Baumbach, R. E. Temperature-Pressure Phase Diagram of Cubic Laves Phase Au<sub>2</sub>Pb. *Phys. Rev. B* **2016**, *93* (4), 045118.

Insert Table of Contents artwork here

